Transport and Communications Science Journal, Vol. 74, Issue 4 (05/2023), 428-444

Transport and Communications Science Journal

PHASE FIELD MODELLING COMBINED WITH OPTIMIZATION ALGORITHM FOR MAXIMIZING THE RESISTANCE IN TWO-PHASE COMPOSITES

Vu Ba Thanh

University of Transport and Communications, No 3 Cau Giay Street, Hanoi, Vietnam

ARTICLE INFO

TYPE: Research Article
Received: 12/12/2022
Revised: 20/04/2023
Accepted: 14/05/2023

Published online: 15/05/2023

https://doi.org/10.47869/tcsj.74.4.4

* *Corresponding author*
Email: thanhvb@utc.edu.vn

Abstract. Recently, the phase field modelling is widely used to model and simulate material damage. In present work, we present a framework of the topology optimization combined with the phase-field modelling with/ without interfacial damage for optimizing the damage resistance of the inclusion-matrix composites. The first phase field method with the interfacial damage described by the phase field variable $d(\mathbf{x})$ and an interfacial phase field variable $\beta(\mathbf{x})$, thus the crack occurs in the interaction between the bulk fracture and the interfacial one; the second phase field method without the interfacial damage describes the crack by using only a damage variable $d(\mathbf{x})$, thus the crack initiates at the points where stress concentration occurs (damage only occurring in the phases). Extended bi-directional evolutionary structural optimization algorithm (BESO) is used to optimize the inclusion distribution in order to reduce its volume while keeping the fracture resistance value of the initial design unchanged. Moreover, the strain tensor orthogonal decompositions are implemented into the phase field methods to improve the inaccuracy in the mechanical behavior of the materials. We compare the inclusion optimal distribution, the crack propagation and the fracture resistance between the proposed models through several numerical examples.

Keywords: phase field modelling, topology optimization, strain orthogonal decomposition, fracture, composite structures.

© 2023 University of Transport and Communications

1. INTRODUCTION

Nowadays, the accurate prediction of the crack nucleation and propagation as well as the load- displacement relationship of the structure, especially when considering the effect of the interfacial damage in the iclusion- matrix composites by the simulation method is a large challenge. Many simulation methods have been developed to describe the damage in structures such as finite element method (FEM), extended finite element method (XFEM), but they can only describe simple cracks but cannot predict the development of the complex cracks or the crack systems. Starting from the theoretical basis of Linear Elastic Fracture Mechanics (LEFM) in solids proposed by Griffith [1] and Irwin [2], the crack will propagate if the energy release rate reaches a critical value. Then, the variational method based on the energy minimization theory is presented by Francfort and Marigo [3], Mumford and Shah [4]. Next, a numerical simulation method based on the criteria of [3, 4] was proposed by Bourdin et al. [5] to describe the complex crack path. Recent studies [6,7] have used the phase field method to simulate the damage of the structure when not considering the influence of the interface between the phases, therefore the cracks are only initiated inside the material phases. Developing the work of [7], Nguyen *et al*. [8] used the phase field method with the interfacial damage. This leads to a crack being initiated in the interaction between the bulk damage in the phases and the interfacial one.

Recently, a theoretical study by He and Shao [9] has shown that in brittle materials, the strain tensor is splitted into the negative and positive parts representing the compressive and tensile behavior in the structure. The negative and positive parts of the strain tensor must satisfy the orthogonal condition which is proved to be an accurate description of the mechanical behavior in the material. This orthogonality requirement is not satisfied in [6,7].

Next, a bi-directional evolutionary structural optimization (BESO) is proposed by Xia and Breitkopf [10] to optimize inclusion distribution in order to reduce its volume while keeping the fracture resistance value of the initial design unchanged. Then, the works [11, 12] have combined BESO algorithm with the phase field method to optimize the fracture resistance and predict the crack system in the structure, but these studies have not considered the strain tensor orthogonal condition presented in He and Shao [9].

Therefore, in this study, the strain orthogonal decomposition is implemented into the phase field method without the interfacial damage [7] and the phase field modelling with the interfacial damage [8] to simulate the fracture of the structure. On the other hand, we have combined BESO algorithm [10] with the simulation method [7] (denoted by the model M1) and the other method [8] (denoted by the model M2) to design the optimal distribution of the inclusion phase. The main advantages of the method are: (i) the orthogonality condition is applied in two phase field methods; (ii) the design of the optimal shape of the inclusion to reduce its volume; (iii) comparison of the crack evolution, the load- displacement curve and the inclusion distribution between two proposed models.

The paper is organized as follows: Section 2 presents two phase field methods [7, 8] which are combined with the orthogonal conditions [9]. Section 3 details the algorithm [10] which is implemented with the aforementioned simulation methods. In Section 4, several numerical examples are shown to demonstrate the capabilities of the proposed methods. Finally, conclusions and perspectives are drawn in Section 5.

2. PHASE FIELD MODELLING WITH THE STRAIN TENSOR DECOMPOSITIONS

An open domain **Ω** contains inclusion- matrix phases (see Figure 1a). In which, Γ^{I} is the interface between these phases and Γ is the crack surfaces, $\partial\Omega$ is the boundary of domain **Ω**. In the phase field method with the interfacial damage [8]: the cracks are approximated by an propagating phase field *d*(**x**) (see Figure 1c) and a fixed scalar variable *β*(**x**) is shown as the geometry of interfaces between different phases (see Figure 1b). In the phase field method without the interfacial damage [8]: Γ is a crack surface in the domain **Ω** (see Figure 1a) and we use only phase field variable *d*(**x**) representing for the crack in the interior of the phases (see Figure 1c).

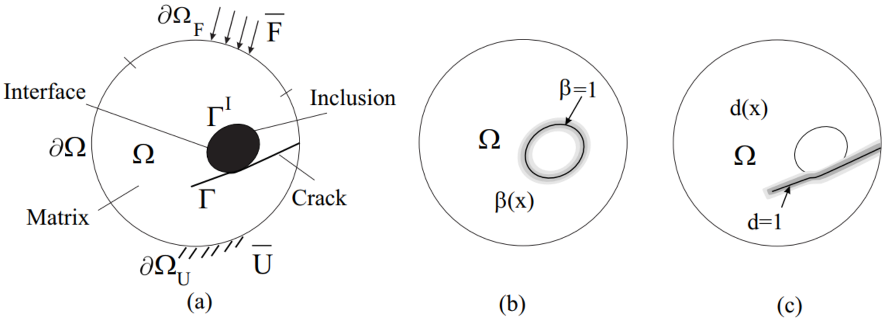

Figure 1. Illustration of phase field crack modeling: (a) a cracked solid containing two-phase, (b) regularized representation of the interfaces by β(**x**); (c) the regularized representation of the crack by *d*(**x**).

2.1. Energy equations in the phase field method

2.1.1. The phase field method with the interfacial damage

In the phase field method with the interfacial damage [8], total energy in the solid is described as follows:

$$\Pi(\mathbf{u},d,\beta)=\int_{\Omega}\bar{\Psi}_{u}^{e}(\mathbf{E}_{e},d)d\Omega+\int_{\Omega}(1-\beta)g_{c}\gamma(d,\nabla d)d\Omega+\int_{\Omega}\bar{\Psi}^{\text{int}}(\;\mathbf{u}\;,\beta)\gamma_{\beta}(\beta,\nabla\beta)d\Omega \qquad (1)$$

where $\gamma(d,\nabla d)=\dfrac{d^{2}}{2l}+\dfrac{l}{2}\nabla d\cdot\nabla d$ and $\gamma_{\beta}(\beta,\nabla\beta)=\dfrac{\beta^{2}}{2l_{\beta}}+\dfrac{l_{\beta}}{2}\nabla\beta\cdot\nabla\beta$ are the crack surface density functions on Γ and Γ^{I}, respectively, g_{c} is the fracture toughness, $\bar{\Psi}^{\text{int}}$ is a strain density function depending on the displacement jump across the interface Γ^{I}. Let $\boldsymbol{\varpi}\approx\;\mathbf{u}\;=h.\nabla\mathbf{u}(\mathbf{x}).\mathbf{n}^{I}$ being the displacement jump at Γ^{I}, *h* is a small scalar parameter related to the displacement jump at Γ^{I}, $\mathbf{n}^{I}$ is the normal vector to Γ^{I}, l and l_{β} are the length parameters representing the width of the smeared cracks on Γ and the width of the smeared interfaces at Γ^{I}, respectively. The variables *d*(**x**) and *β*(**x**) are determined by the Euler–Lagrange equation associated with the variational problem [8].

In the phase field modelling considering the interfacial damage, the strain tensor $\mathbf{E}$ is splitted into the bulk tensor $\mathbf{E}_e$ and the other tensor related to the displacement jump at the interface $\mathbf{E}_{in}$: $\mathbf{E}=\mathbf{E}_e+\mathbf{E}_{in}$. In this problem, $\mathbf{E}_e$ is decomposed into the positive part $\mathbf{E}_e^+$ and the negative part $\mathbf{E}_e^-$ representing the tension and compression parts as follows:

$$\mathbf{E}_e=\mathbf{E}_e^+ +\mathbf{E}_e^- \tag{2}$$

In the work of [8], the different strain density function $\bar{\Psi}_u^e(\mathbf{E}_e,d)$ is defined as follows:

$$\bar{\Psi}_u^e(\mathbf{E}_e,d)=\bar{\Psi}_e^+(\mathbf{E}_e^+)\{g(d)+\kappa\}+\bar{\Psi}_e^-(\mathbf{E}_e^-) \tag{3}$$

where, g(d)=(1-d)^2 is the damage degradation function, $\kappa \ll 1$ is a small parameter to ensure the well-posedness of the system in a partially broken solid.

2.1.2. *The phase field method without the interfacial damage*

In the phase field modelling without the interfacial damage, $\beta\to 0$, this leads to $\gamma_\beta(\beta,\nabla\beta)\to 0$, $\mathbf{E}_{in}\to 0$ and $\mathbf{E}_e\to\mathbf{E}$. Thus, this method becomes the phase field method [7]. In this case, total energy in the cracked solid (1) is defined as:

$$\Pi(\mathbf{u},d)=\int_\Omega \bar{\Psi}_u(\mathbf{E},d)d\Omega+\int_\Omega g_c\gamma(d,\nabla d)d\Omega \tag{4}$$

The strain tensor $\mathbf{E}$ is split into the positive part $\mathbf{E}^+$ and the negative part $\mathbf{E}^-$:

$$\mathbf{E}=\mathbf{E}^+ +\mathbf{E}^- \tag{5}$$

The strain density function $\bar{\Psi}_u$ is composed of the following parts [8]:

$$\bar{\Psi}_u(\mathbf{E},d)=\bar{\Psi}^+(\mathbf{E}^+)\{g(d)+\kappa\}+\bar{\Psi}^-(\mathbf{E}^-) \tag{6}$$

2.2. Introduction of two split operators of the strain tensor

In this work, we present the orthogonal condition to the strain tensor $\mathbf{E}$ of [9]. Two strain energy density functions $\bar{\Psi}^\pm(\mathbf{E}^\pm)$ can be obtained:

$$\bar{\Psi}^\pm(\mathbf{E})=\frac{1}{2}\mathbf{E}^\pm:\left(\mathbb{C}:\mathbf{E}^\pm\right) \tag{7}$$

The orthogonal condition for the positive and negative parts $\mathbf{E}$ is:

$$\mathbf{E}^+:\left(\mathbb{C}:\mathbf{E}^-\right)=0 \tag{8}$$

Let $\bar{\mathbf{E}}^\pm=\mathbb{C}^{1/2}:\mathbf{E}^\pm$ with $\bar{\mathbf{E}}=\bar{\mathbf{E}}^+ +\bar{\mathbf{E}}^-$ and $\bar{\mathbf{E}}^+:\bar{\mathbf{E}}^-=0$ for ensuring the orthogonal condition of strain decomposition, where $\mathbb{C}$ be the fourth-order stiffness tensor.

The orthogonal conditions (7) and (8) of [9] is applied to $\mathbf{E}$ in the phase field method described in section 2.1.2 (denoted by the model M1). To satisfy these orthogonal conditions, we can determine $\bar{\mathbf{E}}^{\pm}$ as (see [13]):

$$\bar{\mathbf{E}}^{\pm} = \sum_{\iota=1}^{D} \left\langle \bar{E}^{\iota} \right\rangle_{\pm} \bar{\mathbf{n}}_{\iota} \otimes \bar{\mathbf{n}}_{\iota} \tag{9}$$

where $\bar{E}^{\iota}$ and $\bar{\mathbf{n}}_{\iota}$ with ι =1, 2,…, D are the ordered eigenvalues and eigenvectors of $\bar{\mathbf{E}}^{\pm}$. This case, called masonry-like model, is initialed by Freddi and Royer-Carfagni [14]. In agreement with this model, the damage is due only to the positive semi-definite symmetric part of the transformed strain $\bar{\mathbf{E}}$. Thus, two strain energy density functions can be obtained:

$$\bar{\Psi}^{\pm}(\mathbf{E}) = \frac{1}{2}\mathbf{E}^{\pm} : \left(\mathbb{C} : \mathbf{E}^{\pm}\right) = \frac{1}{2}\bar{\mathbf{E}}^{\pm} : \bar{\mathbf{E}}^{\pm} \tag{10}$$

From equations (6) and (10), the Cauchy’s stress is written as:

$$\boldsymbol{\sigma} = \frac{\partial \bar{\Psi}_u}{\partial \mathbf{E}} = \left\{ \{g(d)+\kappa\} \left(\overline{\mathbb{Q}}^{+} : \mathbb{C}^{1/2}\right) : \left(\overline{\mathbb{Q}}^{+} : \mathbb{C}^{1/2}\right) + \left(\overline{\mathbb{Q}}^{-} : \mathbb{C}^{1/2}\right) : \left(\overline{\mathbb{Q}}^{-} : \mathbb{C}^{1/2}\right) \right\} : \mathbf{E} \tag{11}$$

From equation (11), two projectors are defined $\overline{\mathbb{Q}}^{\pm} = \dfrac{\partial \bar{\mathbf{E}}^{\pm}}{\partial \bar{\mathbf{E}}}$.

The orthogonal conditions (7) and (8) is applied to the bulk tensor $\boldsymbol{\varepsilon}_e$ in the phase field method with the interfacial in section 2.1.1 (denoted by the model M2). In the model M2, two strain tensor parts $\bar{\mathbf{E}}_e^{\pm}$ are analyzed as:

$$\bar{\mathbf{E}}_e^{\pm} = \sum_{k=1}^{D} \left\langle \bar{E}_e^{k} \right\rangle_{\pm} \bar{\mathbf{n}}_k^{e} \otimes \bar{\mathbf{n}}_k^{e} \tag{12}$$

where $\bar{\mathbf{E}}_e^{\pm} = \mathbb{C}^{1/2} : \mathbf{E}_e^{\pm}$ with $\bar{\mathbf{E}}_e = \bar{\mathbf{E}}_e^{+} + \bar{\mathbf{E}}_e^{-}$ and $\bar{\mathbf{E}}_e^{+} : \bar{\mathbf{E}}_e^{-} = 0,$ and $\bar{E}_e^{k}$ and $\bar{\mathbf{n}}_k^{e}$ with k=1,…, D are the ordered eigenvalues and eigenvectors of $\bar{\mathbf{E}}_e^{\pm}$. In this case, two strain energy density functions can be specified as:

$$\bar{\Psi}_e^{\pm}(\mathbf{E}_e^{\pm}) = \frac{1}{2}\left(\mathbb{C}^{1/2}\,\mathbf{E}_e^{\pm}\right) : \left(\mathbb{C}^{1/2}\,\mathbf{E}_e^{\pm}\right) = \frac{1}{2}\bar{\mathbf{E}}_e^{\pm} : \bar{\mathbf{E}}_e^{\pm} \tag{13}$$

From equations (3) and (13), the Cauchy stress is written as:

$$\boldsymbol{\sigma}_e = \frac{\partial \bar{\Psi}_u^{e}}{\partial \bar{\mathbf{E}}_e} = \left\{ \{g(d)+\kappa\} \left(\overline{\mathbb{P}}^{+} : \mathbb{C}^{1/2}\right) : \left(\overline{\mathbb{P}}^{+} : \mathbb{C}^{1/2}\right) + \left(\overline{\mathbb{P}}^{-} : \mathbb{C}^{1/2}\right) : \left(\overline{\mathbb{P}}^{-} : \mathbb{C}^{1/2}\right) \right\} : \mathbf{E}_e \tag{14}$$

From equation (14), $\overline{\mathbb{P}}^{\pm}$ are two projectors defined as $\overline{\mathbb{P}}^{\pm} = \dfrac{\partial \bar{\mathbf{E}}_e^{\pm}}{\partial \bar{\mathbf{E}}_e}$.

2.3. The phase field and mechanical problems

2.3.1. The phase field and mechanical problems in the model M1

In the model M1, the phase field variable $d(\mathbf{x})$ is determined by solving the weak form equation:

$$\int_{\Omega}\left\{\left(2\mathcal{H}+\frac{g_c}{l}\right)d\delta d+g_c l\nabla d\cdot\nabla(\delta d)\right\}d\Omega=\int_{\Omega}2\mathcal{H}\delta d d\Omega \tag{15}$$

where the strain history function $\mathcal{H}$ is shown as:

$$\mathcal{H}=\max_{\tau\in[0,t]}\left\{\bar{\Psi}^{+}(\mathbf{x},\tau)\right\} \tag{16}$$

By solving the following weak form equation, we can find the displacement variable $\mathbf{u}$ [7]:

$$\int_{\Omega}\boldsymbol{\sigma}:\mathbf{E}(\delta\mathbf{u})d\Omega-\int_{\Omega}\mathbf{f}\cdot\delta\mathbf{u}d\Omega-\int_{\partial\Omega_F}\bar{\mathbf{F}}\delta\mathbf{u}d\Gamma=0 \tag{17}$$

where $\mathbf{f}$ and $\bar{\mathbf{F}}$ are body forces and prescribed traction over the boundary $\partial\Omega_F$.

2.3.2. The phase field and mechanical problems in the model M2

In the phase field problem, the variable $d(\mathbf{x})$ is solved through the weak form expression:

$$\int_{\Omega}\left\{\left(2\mathcal{H}^{e}+(1-\beta)\frac{g_c}{l}\right)d\delta d+(1-\beta)g_c l\nabla d.\nabla(\delta d)\right\}d\Omega=\int_{\Omega}2\mathcal{H}^{e}\delta d d\Omega \tag{18}$$

where the strain history function $\mathcal{H}^{e}$ is shown as:

$$\mathcal{H}^{e}=\max_{\tau\in[0,t]}\left\{\bar{\Psi}_{e}^{+}(\mathbf{x},\tau)\right\} \tag{19}$$

We can find the displacement variable $\mathbf{u}$ (see [8]) by solving the weak form equation:

$$\int_{\Omega}\boldsymbol{\sigma}_e:\mathbf{E}_e(\delta\mathbf{u})d\Omega+\int_{\Omega}\mathbf{t}(\boldsymbol{\varpi})\delta\boldsymbol{\varpi}\gamma_{\beta}(\beta,\nabla\beta)d\Omega-\int_{\Omega}\mathbf{f}.\delta\mathbf{u}d\Omega-\int_{\partial\Omega_F}\bar{\mathbf{F}}\delta\mathbf{u}d\Gamma=0 \tag{20}$$

where $\mathbf{f}$ and $\bar{\mathbf{F}}$ are body forces and prescribed traction over the boundary $\partial\Omega_F$, $\delta\boldsymbol{\varpi}=h\nabla(\delta\mathbf{u}).\mathbf{n}^{I}$. And $\mathbf{t}(\boldsymbol{\varpi})=\dfrac{\partial\bar{\Psi}^{\text{int}}(\boldsymbol{\varpi})}{\partial\boldsymbol{\varpi}}$ is the traction stress at the interface.

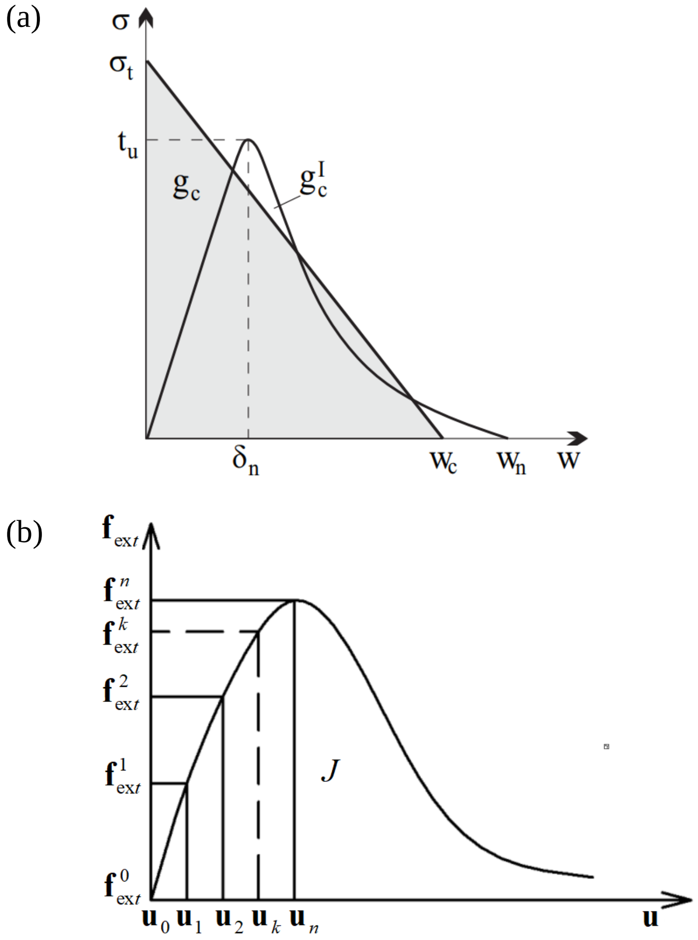

Figure 2. (a) Determination of the fracture toughness g_c and g_c^I; (b) Calculation of the total fracture resistance J.

Then, we set $\mathbf{t}(\boldsymbol{\varpi}) = \left[t_n(\varpi_n), t_t(\varpi_t)\right]^T$ with t_n and t_t are the normal and tangential parts. Here, we determine $t_n = \mathbf{t}(\boldsymbol{\varpi}).\mathbf{n}^I = g_c^I \left(\frac{\varpi_n}{\delta_n}\right)\exp\left(-\frac{\varpi_n}{\delta_n}\right)$ and t_t=0 (see [15]), with $\varpi_n = \boldsymbol{\varpi}.\mathbf{n}^I$ is the normal part of the displacement jump $\boldsymbol{\varpi}$, t_u is the critical fracture strength at Γ^I and $\delta_n = \frac{g_c^I}{t_u \exp(1)}$ is the displacement jump value when $t_n = t_u$ (see [15]). g_c and g_c^I are the fracture toughness in the phase and at the interface (g_c is defined as the total area of the grey triangle and g_c^I is the area under the traction-opening curve of the cohesive law for the interface [15] as depicted in Fig. 2a). In Fig. 2a, $\boldsymbol{\sigma}_t$ is the critical tensive stress in the phases and w_c is the critical crack opening.

3. EXTENDED BESO ALGORITHM FOR OPTIMIZING FRACTURE RESISTANCE

The Young's modulus of element *i* is computed as follows:

$$\mathcal{E}_{\mathrm{i}} = \rho_i \mathcal{E}_{\mathrm{inc}} + (1-\rho_i)\mathcal{E}_{\mathrm{mat}} \tag{21}$$

where $\mathcal{E}_{\mathrm{inc}}$ and $\mathcal{E}_{\mathrm{mat}}$ are the Young's modulus of the inclusion and matrix phases, respectively; ρ_i is a topology design variable with $\rho_i = 0$ if element *i* is the matrix phase, and $\rho_i = 1$ if element *i* is the inclusion phase.

We determine the objective of the total fracture resistance *J* is calculated using numerical integration as (see Fig. 2b):

$$J = \frac{1}{2}\sum_{n=1}^{n_{load}} (\mathbf{f}_{\mathrm{ext}}^{n} + \mathbf{f}_{\mathrm{ext}}^{n-1})^T \Delta\mathbf{u}_n \tag{22}$$

where $\Delta\mathbf{u}_n$ denotes the n^{th} nodal displacement components, and $\mathbf{f}_{\mathrm{ext}}^{n}$ are the external nodal force at the n^{th} load increment.

The topology optimization process subjected to the balance equations to optimize the material volume fractions of the matrix and inclusion phases. Thus, the inclusion volume constraint must satisfy the following system of equations:

$$\begin{cases} \max_{\rho} & : J(\rho, \mathbf{u}, d, \beta) \\ \text{subjected to} & : \mathcal{R} = \mathbf{f}_{ext} - \mathbf{f}_{\mathrm{int}} = 0 \\ & : V(\rho) = \sum \rho_i v_i = V_{req} \\ & : \rho_i = 0 \text{ or } 1, \; i = 1, ..., N_i \end{cases} \tag{23}$$

in which, v_i is the volume of i^{th} element; $V(\rho)$ and V_{req} are the total and required material volumes, respectively; $\mathcal{R}$ denotes the nodal residual force and $\mathbf{f}_{\mathrm{int}} = \rho_i \sum_{i=1}^{N_i} \int_{\Omega_i} \mathbf{B}^T \boldsymbol{\sigma}_e d\Omega_i$, is expressed in terms of the associated topology design variable ρ_i and the Cauchy stress $\boldsymbol{\sigma}_e$; **B** is the shape function matrix derivatives (see [8]).

The objective function *J* can be rewritten in the following form without modifying the original objective value as:

$$J \approx J = \frac{1}{2}\sum_{n=1}^{n_{load}} \left\{ (\mathbf{f}_{\mathrm{ext}}^{n} + \mathbf{f}_{\mathrm{ext}}^{n-1})^T \Delta\mathbf{u}_n + (\boldsymbol{\lambda}_n)^T \mathcal{R}_n + (\boldsymbol{\mu}_n)^T \mathcal{R}_{n-1} \right\} \tag{24}$$

where $\boldsymbol{\lambda}_n$ and $\boldsymbol{\mu}_n$ are the Lagrangian multipliers (n=1, 2,…n_{load}). This equivalence also holds for the sensitivity with respect to changes of the topology design variable ρ_i on element *i*.

$$\frac{\partial J}{\partial \rho_i} = \frac{\partial J}{\partial \rho_i} \tag{25}$$

To formally describe these derivations, we introduce a partitioning of all degrees of freedom into essential (index *I*, associated with Dirichlet boundary conditions) and free (index *K*, remaining degrees of freedom) entries.

$$\frac{\partial \mathbf{u}_n}{\partial \rho_i} = \begin{bmatrix} \mathbf{0} \\ \dfrac{\partial \mathbf{u}_K^n}{\partial \rho_i} \end{bmatrix}, \quad \frac{\partial \Delta \mathbf{u}_n}{\partial \rho_i} = \begin{bmatrix} \mathbf{0} \\ \dfrac{\partial \Delta \mathbf{u}_K^n}{\partial \rho_i} \end{bmatrix}, \quad \mathbf{F}_u^n = \begin{bmatrix} \mathbf{F}_{u,I}^n \\ \mathbf{0} \end{bmatrix}, \quad \frac{\partial \mathbf{F}_u^n}{\partial \rho_i} = \begin{bmatrix} \dfrac{\partial \mathbf{F}_{u,I}^n}{\partial \rho_i} \\ \mathbf{0} \end{bmatrix} \tag{26}$$

From [11, 12], we can determine the final objective function $\frac{\partial J}{\partial \rho_i}$ as follows:

$$\frac{\partial J}{\partial \rho_i} = -\frac{1}{2} \sum_{n=1}^{n_{load}} \left\{ (\boldsymbol{\lambda}_n)^T \int_{\Omega_i} \mathbf{B}^T \boldsymbol{\sigma}_e^n d\Omega_i + (\boldsymbol{\mu}_n)^T \int_{\Omega_i} \mathbf{B}^T \boldsymbol{\sigma}_e^{n-1} d\Omega_i \right\} \tag{27}$$

By the extended BESO method, the target volume of material usage V^k at the current design iteration (k^{th}) is determined by:

$$V^k = \max\left\{V_{req}, (1-ER)V^{k-1}\right\} \tag{28}$$

in which the evolutionary ratio *ER* determines the percentage of material to be removed from the design of the previous iteration. To avoid checkerboard patterns, sensitivity numbers are first smoothed by means of a filtering scheme:

$$\alpha_i = \frac{\sum_{j=1}^{N_i} \mathrm{w}_{ij} \alpha_j}{\sum_{j=1}^{N_i} \mathrm{w}_{ij}}, \text{ and } \mathrm{w}_{ij} = \max\left(0, r_{\min} - \Delta(i, j)\right) \tag{29}$$

where w_{ij} is a linear weight factor, r_{min} is the prescribed filter radius and $\Delta(i, j)$ is the element center-to-center distance between the element *i* and *j*.

The algorithm is summarized as follows:

```
  Initialize the topology design variable $\rho^1$ at the first step
Set $m = 1$, $Err = 1$, $tole = 0.0001$
WHILE $Err > tole$
  Initialize $\mathbf{u}_0(\mathbf{x}), d_0(\mathbf{x}), \mathcal{H}_0\left(\mathcal{H}_0^e\right), J_0, \alpha_0$
  FOR all displacement increments $n = 1, \ldots, n^{load}$
    % Phase field problem
      Given $\{d\}_{n-1}$, $\{\mathbf{u}\}_{n-1}$ and $\mathcal{H}_{n-1}\left(\mathcal{H}_{n-1}^e\right)$
      Compute $\mathcal{H}_n\left(\mathcal{H}_n^e\right)$ from (16) or (19)
      Compute $\{d\}_n(\mathbf{x})$ from (15) or (18)
    % Displcement problem
      Compute $\{\mathbf{u}\}_n(\mathbf{x})$ from (17) or (20)
    % Element sensitivity calculation
      Compute $J^n$ from (24) and $\alpha^n$ from (29)
      $n = n + 1$
  END
  $\alpha^m = \alpha^{n_{load}}$ and $J^m = J^{n_{load}}$
  % Filter scheme of the element sensitivity
  Update $\rho^{m+1}$ with $\alpha^m$
  % Compute convergence
  if $m > 10$
    $Err = \dfrac{\left|\sum_{p=m-9}^{m-5} J^p - \sum_{q=m-4}^{m} J^q\right|}{\sum_{q=m-4}^{m} J^q}$
  else
    $Err = 1$
  end
  $m = m + 1$
END
```

4. NUMERICAL EXAMPLES

The purpose of the following numerical examples is to examine the change of the inclusion distribution at the final design step, the displacement-force curves, and compare the results of the aforementioned models when comparing between M1 and M2. In all the examples, the structures are meshed into uniformly square-shaped bilinear elements. The plane strain assumption have been used. The same finite element discretization is adopted for both displacement and crack phase fields. The material properties are as follows: where $\mathcal{E}_{\text{inc}} = 52\text{GPa}$ and $\mathcal{E}_{\text{mat}} = 10.4\text{GPa}$ are the Young's modulus of the inclusion and matrix and the Poisson's ratio $\nu_{\text{inc}} = \nu_{\text{mat}} = 0.3$ [12].

The fracture toughness of the phases g_c and the interface g_c^I are assumed identical: $g_c = g_c^I = 0.0001$ kN/mm. We choose the fixed value of $l = l_\beta = 1$mm to ensure $l \geq 2h$ (see [16]). The interface fracture strength is set $t_u = 0.01$ GPa. The filter radius $r_{min} = 2h$ and $ER = 5\%$.

4.1. Design of a beam containing an inclusion in the three-point bending test

This example aims to design the optimal distribution of the inclusion phase in the three-point bending test of a beam containing a rectangular inclusion. The geometry and boundary conditions are depicted in Fig. 3. The dimensions of the beam are 30 x 100 mm^2. The domain is uniformly discretized into 60 x 200 elements. The beam contains pre-existing crack whose length is 7.5mm. At the center of the beam on the top side, the monotonic displacement increments of Δu = -0.02 mm are prescribed. The left bottom corner node is fixed in two directions, while the vertical displacement of the right bottom corner node is fixed, and the horizontal displacement is free. In this initial design, the volume fraction of the inclusion phase occupies 14% of the beam. using the extended BESO algorithm, the inclusion phase is gradually reduced to a target volume fraction of 7% in the final design.

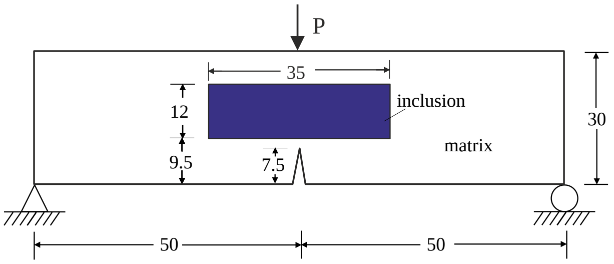

Figure 3. Three point bending test: geometry and boundary conditions.

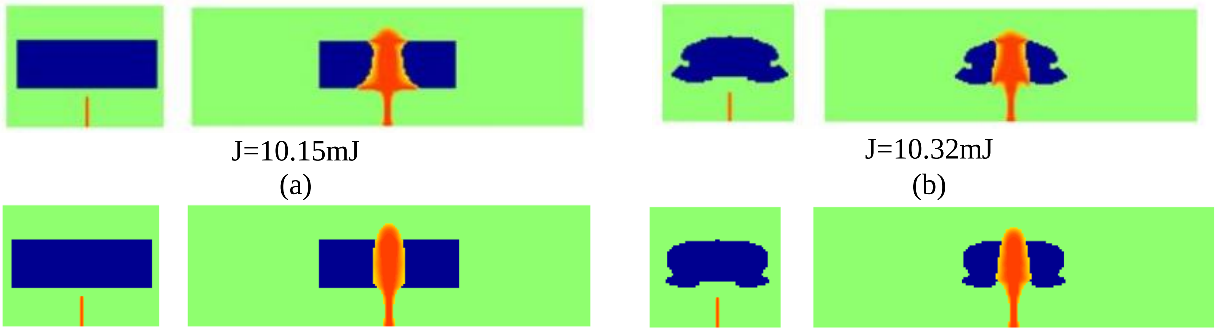
J=10.15mJ
(a)
J=10.32mJ
(b)
J=13.07mJ
(c)
J=13.02mJ
(d)

Figure 4. Comparison of the crack propagation and the inclusion distribution of the initial and final designs related to two models.

Fig. 4 shows the the crack propagation and the inclusion distribution of the initial and final designs related to two models, in which Fig. 4a and Fig. 4c represent the crack in the structure of the initial design of M1 and M2, respectively. Fig. 4b and Fig. 4d are the redistributions of the inclusion phase and crack paths of the final design related to the two aforementioned models. When using the model M2, the crack vertically propagates in the matrix phase and is blocked by the inclusion phase. During the next steps, the crack tries to spread along the horizontal interface but is prevented by the inclusion phase redistributed by using the BESO method. Then, the crack passes through the inclusion phase along the loading direction until the structure is fully broken.

Generally, the crack spreads in the interaction between the interfacial damage and the bulk damage in the phases. When we use the model M1, the crack propagation nucleates from the pre-existing crack, then spreads through the matrix phase and propagates straight to the inclusion phase until the completely damage. We can see the crack propagation and the inclusion distribution of the final designs between two models are completely different.

Fig. 5 shows a comparison of the load-displacement curves of the initial and the final designs related to two models . From these behavior curves, we can determine the corresponding damage resistances *J* of these curves as follows: 10.15mJ for the initial design, 10.32mJ for final design of M2, 13.07mJ for the initial design, 13.02mJ for final design of M1. The damage resistances of M1 is 20.7% larger than the one of M2. We see that the difference between these behavior curves is very large when comparing between the two models. The peak load value in M1 is always higher than M2 because the crack propagates directly into the inclusion phase and is not interacted with the interface between the phases.

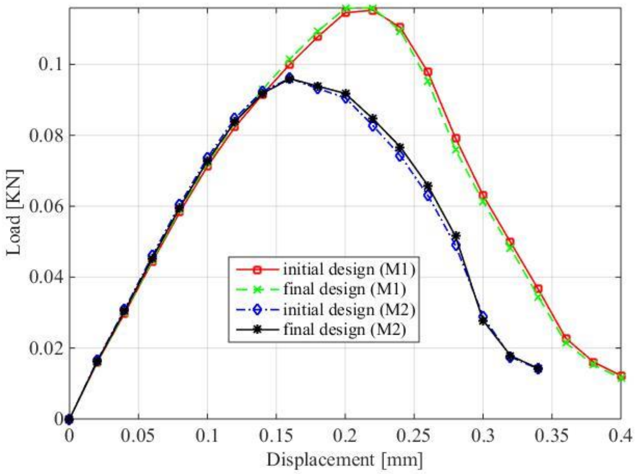

Figure 5. Comparison of the load-displacement curves of the initial and final designs related to two models.

4.2. Design of a plate containing a circular inclusion in the tension test

A plate contains a circular inclusion and a pre-existing crack whose length is 12.5mm. The geometry and loading conditions are presented in Fig. 6. The present paper uses two models of M1 and M2 to optimize the inclusion distribution and reduce its volume while keeping the fracture resistance *J* unchanged.

The dimensions of the domain is 50 x 100 mm^2 and the radius of the inclusion is 12mm. This domain is meshed into 100 x 200 elements. The lower end is fixed in the vertical direction while the horizontal direction is free. The bottom left corner node is fixed in the two directions. At the upper side, the horizontal displacement is free and the vertical displacement is prescribed with a constant incremental displacement $\Delta u = 0.02$ mm during the simulation process. In the initial design, the volume fraction of the inclusion phase is determined to be 9% of the plate. Using the extended BESO algorithm, the inclusion phase is reduced to a target volume fraction of 4.5% of the domain.

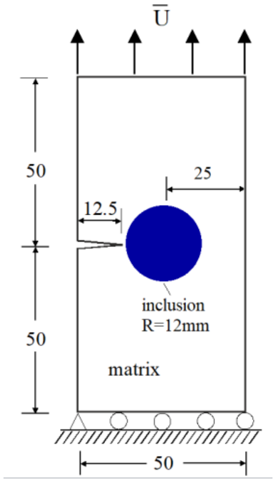

Figure 6. Geometry and boundary conditions.

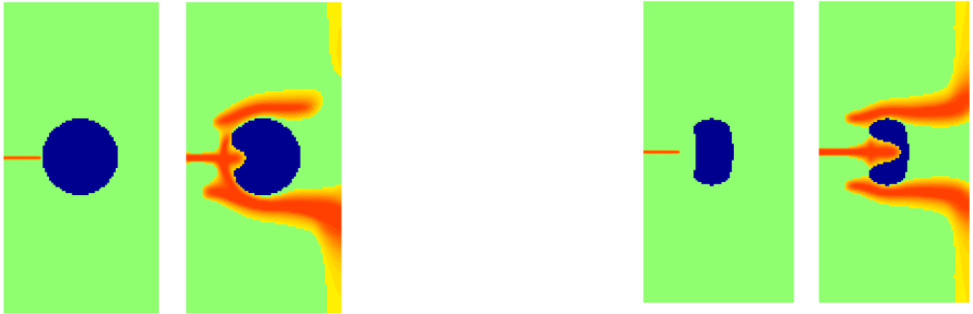

J=34.55mJ
(a)

J=34.02mJ
(b)

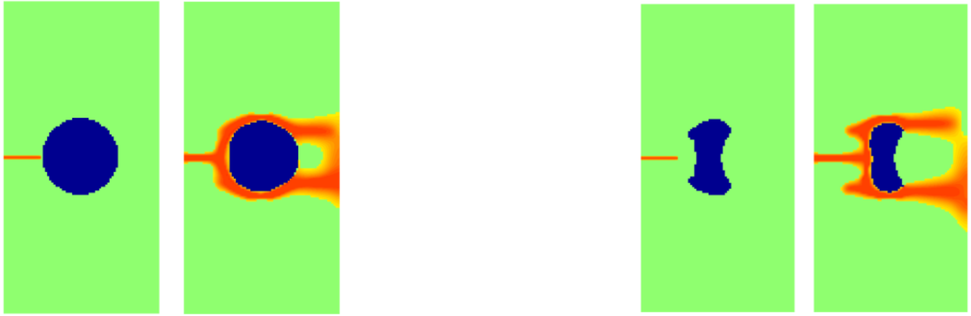

J=21.16mJ
(c)

J=21.37mJ
(d)

Figure 7. Comparison of the crack propagation and the inclusion distribution of the initial and final designs related to two models.

Fig. 7a and Fig. 7c represent the crack in the structure of the initial design of M1 and M2, respectively. Fig. 7b and Fig. 7d are the redistributions of the inclusion phase and crack paths of the final design related to the two models.

When we use the model M1, the crack nucleates from the pre-existing crack and propagates through the matrix phase until the inclusion phase prevents. Then, two other cracks initiate at the top and bottom sides of the inclusion phase where the stress concentration occurs. On the other hand, the crack also tries to pass through the inclusion. The cracks continue to propagate until fully damage in the next displacement increments. In this test, the crack also occurs only in the phases. Therefore, the inclusion phase fraction gradually decreases from 9% to 4.5% by removing the exterior volume of the inclusion phase and retaining the volume part in the center of the inclusion to prevent cracking through the inclusion phase (see Fig. 7b).

When we use the model M2, the crack initiates at the initial crack, propagates horizontally within the matrix phase and is prevented by the inclusion phase. Then, two interfacial cracks nucleate along the bottom and top interfaces between two phases. At the same time, another interfacial crack also initiates at the zone where the crack is blocked by inclusion phase. The use of the BESO algorithm, the volume fraction of the inclusion phase gradually decreases from 9% to 4.5% by removing the surrounding volume of the inclusion. From Fig. 7b and Fig. 7d, it can be seen that, the center zone of the inclusion in M2 is thinner than that of M1 because in M2, the crack can not pass through the inclusion phase in order to develop the interfacial damage.

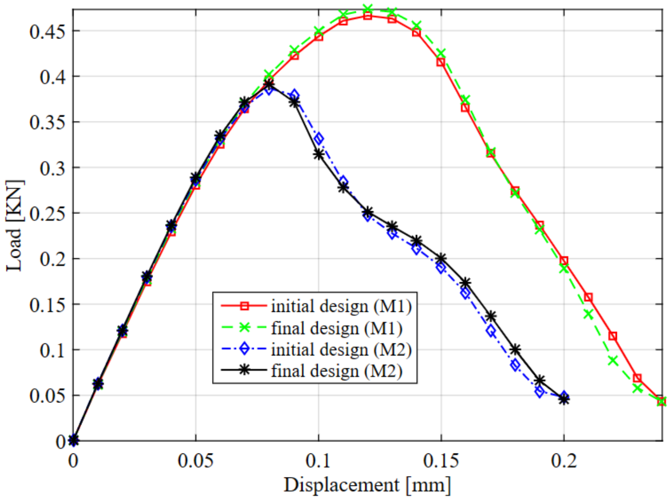

Figure 8. Comparison of the load-displacement curves of the initial and final designs related to two models.

Fig. 8 shows the comparison of the load-displacement curves of the initial and final designs related to two models. We can see that the total damage resistances *J* are as follows: 21.16mJ for the initial design and 21.37mJ for final design of M2; 34.55mJ for the initial design and 34.02mJ for final design of M1. The damage resistance of M1 is 38.75% larger than the one of M2. We see that the difference between these behavior curves is very large when comparing between the two models. In the model M1, the displacement- load curve has only one peak value corresponding to the time at which the crack is nucleated. In the model M2, the crack is still affected in the interaction between the bulk crack and the interfacial one, thus these curves of M2 have two clear peak values.

The extended BESO algorithm combined with the phase field method helps optimize the inclusion phase distribution to reduce its volume fraction while the damage resistane value remains unchanged as depicted in Fig. 5 and Fig. 8 of two aforementioned examples.

5. CONCLUSION AND PERSPECTIVES

In this paper, the strain orthogonal decomposition has been applied into two aforementioned phase field methods to model and simulate the fracture in the inclusion- matrix composites. This condition is illustrated to improve the accuracy in the mechanical behavior in the structure by eliminating the singularity points on the behavior curve and the spurious effect in the structure in the damage process (see [9]).

The extended BESO algorithm combined with the phase field methods help optimize the inclusion phase distribution to reduce its volume fraction while the fracture resistance value remains unchanged. In the model M1, the crack only propagates in the interior of the phases where the stress concentration occurs because we do not consider the effect of the interface, in other words, we consider the adhesion between the phases to be absolute. In the model M2, when considering the effect the interface, the crack develops in the interaction between the bulk damage (represented by the phase field variable d) and the interfacial one (represented by the phase field variable β). Thus, in M2, there are two peak values of the load: (i) the first value represents for the initiation of the crack at pre-existing crack and (ii) the second one represents the nucleation of the crack at the interface. Furthermore, we can see that the fracture resistance of M2 is always smaller than one of M1. This can be explained that the material properties at the interface are smaller than that of the phases. The difference of the crack system between the two models leads to a different optimal distribution of the inclusion phase to prevent the structural failure.

In this study, the models have only optimized for the structures containing a simple inclusion particle. Therefore, in the upcoming study, we will optimize for the structures containing multiple inclusion particles with their random arrangement. Then, we will give an experimental procedure of the actual samples to compare with the corresponding simulation results.

ACKNOWLEDGMENT

This research is funded by University of Transport and Communications (UTC) under grant number T2022-CT-005TD.

REFERENCES

[1]. G. A. Griffith, The phenomena of rupture and flow in solid, Philosophical Transaction of the Royal Society London Series A, 221 (1921) 163-198. https://doi.org/10.1098/rsta.1921.0006

[2]. G. R. Irwin, Analysis of stress and strains near the end of a crack traversing a plate, J. Appl. Mech, 24 (1957) 361-364.

[3]. G. A. Francfort, J. J. Marigo, Revisiting brittle fracture as an energy minimization problem, J. Mech. Phys. Solids, 46 (1998) 1319-1342. https://doi.org/10.1016/S0022-5096(98)00034-9

[4]. D. Mumford, J. Shah, Optimal approximations by piecewise smooth functions and associated variational problems, Commun. Pure. Appl. Math, 42 (1989) 577-685. https://doi.org/10.1002/cpa.3160420503

[5]. B. Bourdin, J. J. Marigo, C. Maurini, P. Sicsic, Morphogenesis and propagation of complex cracks induced by thermal shocks, Phys. Rev. Lett, 112 (2014) 014301. https://doi.org/10.1103/PhysRevLett.112.014301

[6]. C. Miehe, M. Hofacker, F. Welschinger, A phase field model for rate-independent crack propagation: robust algorithmic implementation based on operator splits, Comput. Methods Appl. Mech. Eng, 199 (2010) 2765-2778. https://doi.org/10.1016/j.cma.2010.04.011

[7]. T. T. Nguyen, J. Yvonnet, Q. Z. Zhu, M. Bornert, C. Chateau, A phase field method to simulate crack nucleation and propagation in strongly heterogeneous materials from direct imaging of their microstructure, Eng. Fract. Mech, 139 (2015) 18-39. https://doi.org/10.1016/j.engfracmech.2015.03.045

[8]. T. T. Nguyen, J. Yvonnet, Q. Z. Zhu, M. Bornert, C. Chateau, A phase-field method for computational modeling of interfacial damage interacting with crack propagation in realistic microstructures obtained by microtomography, Comput. Methods Appl. Mech. Eng, 312 (2016) 567–95. https://doi.org/10.1016/j.cma.2015.10.007

[9]. Q. C. He, Q. Shao, Closed-form coordinate-free decompositions of the two-dimensional strain and stress for modeling tension-compression dissymmetry, J. Appl. Mech, 86 (2019) 031007. https://doi.org/10.1115/1.4042217

[10]. L. Xia, P. Breitkopf, Recent advances on topology optimization of multiscale nonlinear structures, Arch. Comput. Methods Eng, 24 (2017) 227–249. https://doi.org/10.1007/s11831-016-9170-7

[11]. L. Xia, D. C. Da, J. Yvonnet, Topology optimization for maximizing the fracture resistance of quasi-brittle composites, Comput. Methods Appl. Mech. Eng, 332 (2018) 234–254. https://doi.org/10.1016/j.cma.2017.12.021

[12]. D. C. Da, J. Yvonnet, L. Xia, G. Li, Topology optimization of particlematrix composites for optimal fracture resistance taking into account interfacial damage, Int. J. Numer. Methods Eng, 115 (2018) 604–626. https://doi.org/10.1002/nme.5818

[13]. B. T. Vu, Modeling and simulation of damage in anisotropic materials by the phase-field method, PhD Thesis, Paris-Est University, France, (2021).

[14]. G. Lancioni, G. Royer-Carfagni, The variational approach to fracture mechanics. a practical application to the French Panthéon in Paris, J. Elasticity, 95 (2009) 1-30. https://doi.org/10.1007/s10659-009-9189-1

[15]. C. V. Verhoosel, R. de Borst, A phase-field model for cohesive fracture, Int. J. Numer. Methods Engrg, 96 (2013) 43–62. https://doi.org/10.1002/nme.4553

[16]. T. T. Nguyen, J. Yvonnet, M. Bornert, C. Chateau, K. Sab, R. Romani, R. Le Roy, On the choice of parameters in the phase field method for simulating crack initiation with experimental validation, Int. J. Fracture, 197 (2016) 213-226. https://doi.org/10.1007/s10704-016-0082-1